scientific reports

Check for updates

OPEN

Peristaltic flow in the glymphatic system

Francesco Romanò[1]✉, Vinod Suresh[2], Peter A. Galie[3] & James B. Grotberg[4]

The flow inside the perivascular space (PVS) is modeled using a first-principles approach in order to investigate how the cerebrospinal fluid (CSF) enters the brain through a permeable layer of glial cells. Lubrication theory is employed to deal with the flow in the thin annular gap of the perivascular space between an impermeable artery and the brain tissue. The artery has an imposed peristaltic deformation and the deformable brain tissue is modeled by means of an elastic Hooke's law. The perivascular flow model is solved numerically, discovering that the peristaltic wave induces a steady streaming to/from the brain which strongly depends on the rigidity and the permeability of the brain tissue. A detailed quantification of the through flow across the glial boundary is obtained for a large parameter space of physiologically relevant conditions. The parameters include the elasticity and permeability of the brain, the curvature of the artery, its length and the amplitude of the peristaltic wave. A steady streaming component of the through flow due to the peristaltic wave is characterized by an in-depth physical analysis and the velocity across the glial layer is found to flow from and to the PVS, depending on the elasticity and permeability of the brain. The through CSF flow velocity is quantified to be of the order of micrometers per seconds.

Cerebrospinal fluid serves as a sink for metabolic waste products generated in the brain. The pathway for CSF transport in the brain interstitium has been a puzzle. Recent imaging experiments using in vivo two-photon microscopy have lent support to the hypothesis that CSF enters the brain from the subarachnoid space along the perivascular sheaths surrounding penetrating arteries and 'leaks' out into the interstitium across a permeable layer of glial (astrocyte) cells. From there, it is cleared into the perivascular sheaths around veins and the pulsation of the cerebral arteries are identified as an important driver for the transport of CSF into the brain interstitium[1,2]. Since convective bulk flow of the CSF between these ingress and egress pathways facilitates the clearance of solutes and metabolic waste products from brain tissue, dysfunctions in CSF transport may have implication for a range of neurological conditions such as intracranial hypertension and protein clearance in Alzheimer's disease and Parkinson's disease. Empirical studies[2–4] indicate that CSF transport is affected by the elastic properties of vessel walls, water permeability of brain tissue and pulsatility of blood flow. However, the difficulty of measuring these parameters in vivo necessitates modeling-based approaches to improve our understanding of fluid transport in the brain. Therefore, the aim of this study is to develop a mathematical model of perivascular transport that provides insight into how these factors alter the direction and magnitude of CSF flow. Since we aim at deriving a leading-order characterization of the CSF flow, the impact of ciliated boundaries and non-Newtonian effects[5–7] will be neglected in our model.

The model described here builds upon previous approaches to calculate perivascular fluid flow in idealized geometries. Wang and Olbricht[8] studied axial flow and transport in an annulus with impermeable boundaries, but did not address fluid exchange with the interstitium[9]. Kyrtsos and Baras modeled protein clearance from the interstitium using a compartmental model in which CSF velocity was an input parameter and was assumed to be inversely proportional to vessel stiffness[10]. Cerebral MRI visualizations of a live rat have been used by Ratner et al.[11] to find the direction of the glymphatic flow. Moreover, they made use of a purely diffusive model to estimate the liquid flow through the healthy brain of a rat and reproduced the main experimental features by means of an Optimal Mass Transfer approach which could also estimate the diffusion tensor based on the dynamic flow rate. By means of numerical simulations, Asgari et al.[12] claimed that the arterial pulsation due to the peristaltic wave cannot be the tribological driving force responsible of the interstitial solute transport. They address the role of dispersion transport, which is a combination of local mixing and diffusive effects in the para-arterial space.

[1]Univ. Lille, CNRS, ONERA, Arts et Métiers Institute of Technology, Centrale Lille, UMR 9014 - LMFL - Laboratoire de Mécanique des Fluides de Lille - Kampé de Fériet, 59000 Lille, France. [2]Auckland Bioeng. Inst. and Dept. Eng. Sci., University of Auckland, 70 Symonds Street, Bldg 439, Auckland 1010, New Zealand. [3]Dept. Biomed. Eng., Rowan University, 201 Mullica Hill Rd, Glassboro, NJ 08028, USA. [4]Dept. Biomed. Eng., University of Michigan, 2123 Carl A. Gerstacker Building, 2200 Bonisteel Boulevard, Ann Arbor, MI 48109-2099, USA. ✉email: francesco.romano@ensam.eu

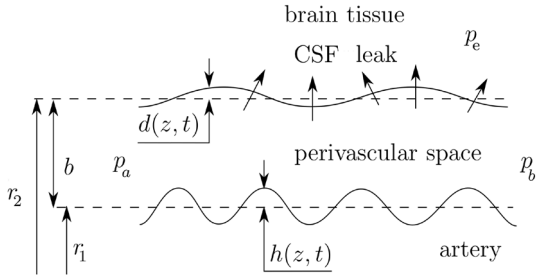

Figure 1. Sketch of the perivascular space between the brain tissue and the artery.

A very different conclusion has been drawn by Aldea et al.[13], who proposed a multiscale model of the arteries dealing with the basement membrane as a deformable fluid-filled, poroelastic medium. They rather concluded that the vasomotion-driven intramural periarterial drainage is compatible with experimental observations.

Jin et al.[14] modeled the glymphatic system from para-arterial to paravenous cerebrospinal fluid through brain extracellular space. They investigated the glymphatic mechanism for solute clearance in brain by modeling diffusive and convective transport in the cerebral extracellular space, focusing on the short-range transport between para-arterial and paravenous spaces. Based on the numerical simulations of their model, they concluded that the convective transport is not affected by the pressure fluctuations and requires a strong pressure gradient to be significant. Moreover, they found that the convective transport is also fairly insensitive to astrocyte endfoot water permeability and that diffusion transport suffices to explain the experimental data of the transport studies in brain parenchyma. Similarly, Faghih and Sharp[15] use a one-dimensional steady, pressure-driven branching flow model to analyze the hydraulic resistance of arterial membranes. They found that the resistance of the periarterial tree is too great to account for physiological estimates of the CSF leakage rate, and that a combined route through the paraarterial and paravenous spaces would also be unlikely based on the magnitude of the transmantle pressure. A similar approach was employed by Rey and Sarntinoranont[16], who made use of two resistance network models to study the effect of pulsating flows. They estimated that the peak fluid velocity in the PVS and parenchyma increases with the pulse amplitude and the vessel size, making the convective solute transport less and less relevant.

Our model derives a leading order approximation of the Navier–Stokes equation which is based on lubrication theory and includes the effect of a peristaltic wave in the artery and the deformability of the brain tissue. A further justification of the negligible importance of convective transport compared to diffusion effects in the PVS will be derived from first principles, motivating such a conclusion by dimensional analysis considerations. Thereafter, focusing on CSF exchange between the perivascular space and brain interstitium, we compute the leak velocity using our first-principles approach.

Model

Geometry. The CSF-filled perivascular space was modeled as a thin annular gap between an elastic, impermeable artery and a brain tissue (Fig. 1). An elastic, permeable glial boundary separates the PVS from the brain tissue. The glial boundary is modeled with a linear elastic wall law and we do not solve for the flow in the artery. Instead, the peristaltic wave deformation of the artery is prescribed as a travelling wave. The interstitial pressure was assumed to be constant and was used as the reference pressure. Linear elastic tube laws were used to relate the deformations of the solid boundaries to the pressure difference across them. Governing equations were simplified using lubrication theory.

The thickness of the PVS is b, the average radius of the artery and the average inner radius of the brain tissue are r_1 and r_2, respectively. The deformation about the average radii are $h(z,t) = \bar{h}\sin[2\pi/\lambda(z-ct)]$ and $d(z,t)$, where h is the imposed deformation of the travelling peristaltic wave, $\bar{h}$, λ and c its amplitude, wavelength and velocity, respectively, z is the traveling (axial) direction, t the time, and d the glial boundary deformation. The pressure in the brain tissue is p_e, whereas p_a and $p_b < p_a$ are assumed as pressures at the extrema of the PVS.

Governing equations. The Navier–Stokes and continuity equations in dimensional form read

$$\frac{\partial u}{\partial t} + u\frac{\partial u}{\partial r} + w\frac{\partial u}{\partial z} = -\frac{1}{\rho}\frac{\partial p}{\partial r} + \frac{\mu}{\rho}\left(\frac{1}{r}\frac{\partial u}{\partial r} + \frac{\partial^2 u}{\partial r^2} + \frac{\partial^2 u}{\partial z^2}\right), \tag{1a}$$

$$\frac{\partial w}{\partial t} + u\frac{\partial w}{\partial r} + w\frac{\partial w}{\partial z} = -\frac{1}{\rho}\frac{\partial p}{\partial z} + \frac{\mu}{\rho}\left(\frac{1}{r}\frac{\partial w}{\partial r} + \frac{\partial^2 w}{\partial r^2} + \frac{\partial^2 w}{\partial z^2}\right), \tag{1b}$$

$$\frac{1}{r}\frac{\partial (ru)}{\partial r} + \frac{\partial w}{\partial z} = 0, \tag{1c}$$

where $\vec{u} = (u, w)$ denotes the velocity field in cylindrical coordinates, p is the pressure, $\vec{r} = (r, z)$ and t are the spatial and temporal coordinates, respectively, ρ is the density of the fluid flowing in the perivascular space, μ its dynamic viscosity.

Equation (1) are then scaled with

$$r = bR, \quad z = \lambda Z, \quad t = \frac{T}{\omega}, u = b\omega U, \quad w = \lambda\omega W, \quad p = \frac{\mu\omega}{\varepsilon^2}P, \tag{2}$$

where $\omega = c/\lambda$ is the frequency of peristaltic wave in the artery, b is the thickness of the perivascular fluid film, and $\varepsilon = b/\lambda$. The non-dimensional continuity and Navier–Stokes equations read

$$\varepsilon^3 \,\mathrm{Re}\left(\frac{\partial U}{\partial T} + U\frac{\partial U}{\partial R} + W\frac{\partial U}{\partial Z}\right) = -\frac{\partial P}{\partial R} + \varepsilon^2\left(\frac{1}{R}\frac{\partial U}{\partial R} + \frac{\partial^2 U}{\partial R^2} + \varepsilon^2\frac{\partial^2 U}{\partial Z^2}\right), \tag{3a}$$

$$\varepsilon \,\mathrm{Re}\left(\frac{\partial W}{\partial T} + U\frac{\partial W}{\partial R} + W\frac{\partial W}{\partial Z}\right) = -\frac{\partial P}{\partial Z} + \left(\frac{1}{R}\frac{\partial W}{\partial R} + \frac{\partial^2 W}{\partial R^2} + \varepsilon^2\frac{\partial^2 W}{\partial Z^2}\right), \tag{3b}$$

$$\frac{1}{R}\frac{\partial (RU)}{\partial R} + \frac{\partial W}{\partial Z} = 0, \tag{3c}$$

where $\mathrm{Re} = \varepsilon\rho\omega b^2/\mu$ is the Reynolds number.

The mathematical problem (3) is closed by the boundary conditions

$$Z = 0 : P = P_a, \tag{4a}$$

$$Z = L : P = P_b, \tag{4b}$$

$$R = R_1 + H : U = \partial_T H, \qquad W = 0, \tag{4c}$$

$$R = R_1 + 1 + D : \vec{U}\cdot\vec{n} = \partial_T D + M_e(P - P_e), \tag{4d}$$

$$\vec{U}\cdot\vec{t} = 0, \tag{4e}$$

$$D = (P - P_e)/E_e, \tag{4f}$$

where $M_e = k_g\mu/b\varepsilon^2$, P_e is the non-dimensional pressure at the glial boundary and k_g the permeability of the brain tissue, $E_e = E_g\varepsilon^2/\mu\omega(R_1 + 1)$ and E_g the Young's modulus of the brain tissue. $H = h/b = \bar{H}\sin[2\pi(Z - T)]$ is the imposed deformation of the peristaltic wave of the artery and $\bar{H} = \bar{h}/b$ its amplitude measured from the middle line $R_1 = r_1/b$. $D = d/b$ is the deformation of the peristaltic layer at the boundary with the brain tissue; it is measured from the middle line $R_2 = r_2/b = R_1 + 1$. The normal and tangent unit vector to the glial boundary are denoted by $\vec{n}$ and $\vec{t}$.

Thin film approximation. Assuming that $\varepsilon \ll 1$, i.e. the wavelenth λ of the peristaltic wave is much larger than the film thickness b, we expand the pressure, the velocity field and the deformation D with the following polynomial series

$$P = P_0 + \varepsilon P_1 + \varepsilon^2 P_2 + \ldots, \tag{5a}$$

$$U = U_0 + \varepsilon U_1 + \varepsilon^2 U_2 + \ldots, \tag{5b}$$

$$W = W_0 + \varepsilon W_1 + \varepsilon^2 W_2 + \ldots, \tag{5c}$$

$$D = D_0 + \varepsilon D_1 + \varepsilon^2 D_2 + \ldots, \tag{5d}$$

where the subscript 0 denotes the solution at the leading order term, $\mathcal{O}(\varepsilon^0)$, 1 refers to the linear correction in ε, $\mathcal{O}(\varepsilon^1)$, 2 indicates the quadratic correction in ε, $\mathcal{O}(\varepsilon^2)$, and so on.

If $\mathrm{Re} = \mathcal{O}(1)$ or smaller, the leading order continuity and Navier–Stokes equations read

$$\frac{\partial P_0}{\partial R} = 0, \tag{6a}$$

$$\frac{\partial P_0}{\partial Z} = \frac{1}{R}\frac{\partial W_0}{\partial R} + \frac{\partial^2 W_0}{\partial R^2}, \tag{6b}$$

$$\frac{1}{R}\frac{\partial (RU_0)}{\partial R} + \frac{\partial W_0}{\partial Z} = 0. \tag{6c}$$

The system (23) is completed by the boundary conditions at leading order

$$Z = 0 : P_0 = P_a, \tag{7a}$$

$$Z = L : P_0 = P_b, \tag{7b}$$

$$R = R_1 + H : U_0 = \partial_T H, \qquad W_0 = 0, \tag{7c}$$

$$\begin{aligned} &R = R_1 + 1 + D_0 : \vec{n} = (n_r, n_z) = (1, 0), \\ &\vec{t} = (t_r, t_z) = (0, 1), \end{aligned} \tag{7d}$$

$$U_0 = M_e(P_0 - P_e) + \frac{1}{E_e}\frac{\partial (P_0 - P_e)}{\partial T}, \tag{7e}$$

$$W_0 = 0, \tag{7f}$$

$$D_0 = \frac{P_0 - P_e}{E_e}. \tag{7g}$$

More details of the model derivation are given in the section Methods. We however remark that leading order boundary conditions do not include any axial flow at the walls, i.e. $W_0 = 0$ along the boundaries. For more details about the effect of the axial flow in the glymphatic system, we refer to Albargothy et al.[17].

The leading order term of the r-momentum implies that P_0 is only function of Z and T and, integrating in r the z-momentum, W_0 reads

$$W_0 = \frac{R^2}{4}\frac{\partial P_0}{\partial Z} + C_1 \ln(R) + C_2, \tag{8}$$

where $C_1 = C_1(Z, T)$ and $C_2 = C_2(Z, T)$.

Plugging (8) in the continuity equation and integrating in R, we derive the form of U_0

$$U_0 = \frac{C_3}{R} - \frac{R^3}{16}\frac{\partial^2 P_0}{\partial Z^2} - \frac{R}{4}[2\ln(R) - 1]\frac{\partial C_1}{\partial Z} - \frac{R}{2}\frac{\partial C_2}{\partial Z}, \tag{9}$$

where $C_3 = C_3(Z, T)$.

Applying the no-slip boundary conditions at the inner boundary ($R = R_1 + H$), i.e. $U_0 = \partial_T H$ and $W_0 = 0$, and the permeable boundary condition at the outer boundary ($R = R_1 + 1 + D$), i.e. $U_0 = M_e(P_0 - P_e) + E_e^{-1}\partial_T(P_0 - P_e)$ and $W_0 = 0$, the functions C_1, C_2 and C_3 are expressed in terms of P_0 and a second-order differential equation is derived for P_0

$$\frac{\partial P_0}{\partial T} + A_0\frac{\partial^2 P_0}{\partial Z^2} + A_1\frac{\partial P_0}{\partial Z} + A_2 P_0 = \left[\frac{E_e(R_1 + H)}{R_1 + 1 + D_0}\right]\frac{\partial H}{\partial T} + E_e M_e P_e + \frac{\partial P_e}{\partial T}. \tag{10}$$

We refer to the section Methods for the definition of A_0, A_1, A_2. The initial condition for P_0 is set to be the linear function consistent with the boundary conditions

$$P_0(T = 0) = P_a(T = 0) + [P_b(T = 0) - P_a(T = 0)]Z/L. \tag{11}$$

Equation (10) is solved numerically by making use of a collocation spectral method in Z-direction and discretizing in time by implicit Euler method. The time step employed to discretize in time is always set equal to $\Delta t = 10^{-2}$ and 1000 Chebyshev–Gauss–Lobatto nodes are used in Z. Further details about the numerical method we chose and its implementation in our solver are reported in the section Methods. In order to avoid non-linearities in the discretization algorithm, the explicit outer-wall deformation D_0^n is employed when computing the solution at time t_{n+1}.

We remark that taking into account the recent study by Mestre et al.[4], the annular space around blood vessels in the brain is not uniform in thickness. In this sense, our axisymmetric approach represents a simplification of the perivascular space geometry assuming that the averaged cross-sectional radius is sufficient to capture the leading-order effects of the CSF dynamics. We stress that such an assumption is at the core of the simplified one-dimensional time-dependent partial differential Eq. (10). Including a non-uniform deformation of the gap cross-section would require a non-trivial extension of the model as the pressure, the glial boundary deformation and the flow velocity should depend by all the three spatial coordinates, i.e. R, Z and Φ. The resulting system of PDEs would make the extended model far more complex to solve and we expect it would not provide major improvements in the order-of-magnitude estimate of the steady streaming across the glial boundary.

Parameter	Description (definition)	Estimated range
Re	Reynolds number $(\varepsilon\rho\omega b^2/\mu)$	$[5\times10^{-12},\ 2\times10^{-4}]$
ε	Perivascular film thickness (b/λ)	$[10^{-6},\ 3.75\times10^{-2}]$
R_1	Inner radius of the perivascular layer (r_1/b)	$[0.7,\ 10^3]$
$\bar{H}$	Amplitude of the peristaltic wave $(\bar{h}/b)$	$[8\times10^{-4},\ 0.5]$
L	Perivascular length (l/λ)	$[2,\ 20]$
M_e	Permeability of the brain tissue $(k_g\mu/b\varepsilon^2)$	$[10^{-2},\ 10]$
E_e	Stiffness of the brain tissue $(E_g\varepsilon^2/\mu\omega(R_1+1))$	$[2\times10^{-10},\ 0.2]$

Table 1. Range of the non-dimensional groups for the thin-film problem between an artery and a brain tissue.

Results

Physiological parameters.

Physiologically relevant parameters for the thin liquid film of interest are derived from the literature. Xie et al.[18] estimates the intracranial pressure to be about 2×10^3 Pa, in accordance with Sakka et al.[19], who report $p_e\in[1300,\ 2000]$ Pa. Assuming $P_e=P_b=0$ as reference pressure in our model, P_a will then be considered in the range $P_a\in[5\times10^{-7},5\times10^2]$. Wang and Olbricht[8] report the values measured in previous studies for: the peristaltic wave frequency $\omega\approx5$ Hz[3], the inner radius of the perivascular layer $r_1\approx10^{-5}$ m[20], the outer radius of the perivascular layer $r_2\approx1.1\times10^{-5}$ m[21] (which result in a perivascular film thickness $b\approx10^{-6}$ m), the peristaltic wave amplitude $\bar{h}\in[1.25,\ 5]\times10^{-7}$ m[22], the peristaltic wave speed $c\approx1$ m s^{-1}[20,23,24] (which result in a peristaltic wavelength $\lambda\approx0.2$ m), and the dynamic viscosity $\mu=9\times10^{-4}$ Pa s[25]. Plus, the fluid density is comparable to the one of water $\rho\approx\rho_{water}=10^3$ kg m^{-3}. Other values of the artery radius ($r_1\in[10^{-4},\ 10^{-3}]$ m) are reported in Thorin-Trescases et al.[26] Moreover, considering that the artery wall thickness t_a is 10 to 100 times smaller than r_1, i.e. $t_a\in[10^{-6},\ 10^{-5}]$ m[27], that the elastic modulus of the artery wall is $E_a\in[10^5,\ 10^6]$ N m^{-2} and that the wall density is $\rho_a\approx10^3$ kg m^{-3}, the elastic wave speed is $c_a=\sqrt{E_at_a/2r_1\rho_a}\in[0.2,\ 7]$ m s^{-1}. Considering the relationship given by Atabek[28], i.e. $c\in[0.1,\ 0.5]c_a$, an estimated range of the wave speed of the peristaltic wave can be proposed, which includes the estimate of Wang and Olbricht[8]: $c\in[0.02,3.5]$ m s^{-1} resulting in a range for the peristaltic wavelength $\lambda\in[0.004,\ 0.7]$ m, which includes the previous estimate $\lambda\approx0.2$ m. Another estimate of b is given by Iliff et al.[1], who reports $b=10^{-5}$ m, and by Jin et al.[14], who reports $b=1.5\times10^{-4}$ m. Finally, The elastic modulus and the permeability of the brain tissue are $E_g\approx0.01E_a\in[10^3,\ 10^4]$ Pa and $k_g\approx10^{-11}$ m Pa^{-1} s^{-1}, respectively[29,30]. Based on these parameters, the range of the non-dimensional groups of interest for our study is derived and reported in Table 1. From Table 1 it is clear that the leading-order thin-film approach is a very good approximation for our problem since $\varepsilon\ll1$ and Re $\ll1$. Higher-order corrections in ε and inertial effects due to Re are, therefore, substantially negligible.

Parametric study. Based on the physiologically relevant parameters, we carried out numerical simulations for the following range of non-dimensional groups

$$R_1\in[10,\ 1000],\quad \bar{H}\in[0,\ 0.2],\quad L\in[2,\ 20],\quad M_e\in[0.1,\ 5],\quad E_e\in[0.01,\ 1]. \tag{12}$$

We remark that the range of the glial boundary elasticity parameter E_e has been restricted to vary over 3 rather than 10 orders of magnitude, as indicated in Table 1. Indeed, when the Young modulus of the brain tissue is very small, i.e for the softest brain tissue parameters reported in Table 1, $E_e\ll1$, a small pressure difference across the glial boundary is sufficient to induce significant deformations, hence (7e) reduces to $P_0\approx P_e$ and $U_0\approx0$. As a result, in the limit $E_e\to0$, (10) becomes an instantaneous equation that cannot admit any through flow. For these reasons, we limited our parametric studies to Young moduli related to the most interesting CSF dynamics that can admit steady streaming, i.e. $E_e\in[0.01,\ 1]$.

All the simulations are carried out for $t_{fin}=100$ with $\Delta t=10^{-4}$ and the results are interpreted in terms of brain tissue deformation D_0 and through-flow velocity $U_0-\partial_TD_0$. Since the solution is time-dependent, the corresponding time averages $\langle D_0\rangle$ and $\langle U_0-\partial_TD_0\rangle$ are analyzed, averaging over $t\in[50,100]$ in order to get rid of the initial transient effects. The boundary conditions in pressure are

$$P_a=10^{-3},\qquad P_e=0,\qquad P_b=0. \tag{13}$$

It is remarkable that, in our model framework, the pressure distribution $P_0(Z,T)$, the deformation of the brain tissue $D_0(Z,T)$ and the through-flow velocity $U_e(Z,T)=U_0|_{R=R_1+1+D_0}-\partial_TD_0$ can be derived from each other taking into account the permeability parameter M_e and the elasticity parameter E_e

$$U_e=M_eP_0,\quad D_0=E_e^{-1}P_0, \tag{14}$$

hence, analyzing the results in terms of one among P_0, U_e or D_0 provides information about all three these quantities. A direct implication of it is the pressure boundary conditions play the role of boundary constraints for U_e and D_0, too. Hence, given an elasticity parameter E_e, regardless of M_e, $\bar{H}$, L and R_1, the brain tissue deformation at $Z=0$ will always be $D_0|_{Z=0}=E_e^{-1}P_a$ and at $Z=L$ $D_0|_{Z=L}=0$. With the same argument, fixing M_e and regardless of E_e, $\bar{H}$, L and R_1, the through-flow velocity on the left will always be $U_e|_{Z=0}=M_eP_a$ and on the right $U_e|_{Z=L}=0$.

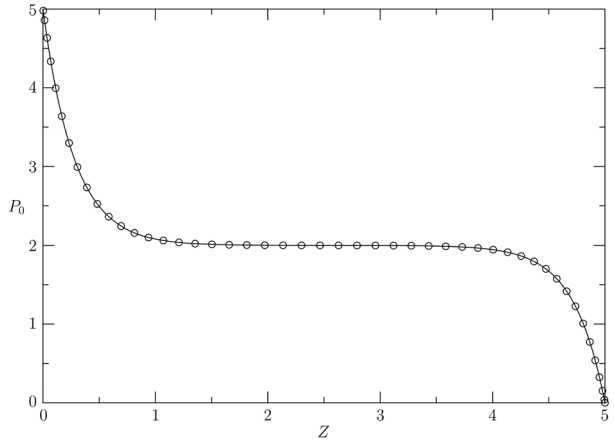

Figure 2. Comparison between the exact steady solution of (16) (solid line) valid for $E_e \to \infty$ and $\bar{H} = 0$ and the corresponding numerical solution of (10) (circles) evaluated at $t = 1$ and computed for $\bar{H} = 0$ and $E_e = 10^5$. The other parameters of the comparison are $P_e = 2$, $P_a = 5$, $P_b = 0$, $M_e = 1$, $L = 5$ and $R_1 = 5$.

Vanishing peristaltic wave. We first consider all the cases with $\bar{H} = 0$, since the flow reaches a steady state ($\partial_T D_0 = \partial_T P_0 = 0$) and it can be well understood taking into account the exact solution reported for the flow in an annular pipe with a permeable wall. This represents an asymptotic limit of our problem and can therefore be used as a validation case for our solver. Taking the limit of $\bar{H} \to 0$, $E_e \to \infty$ and assuming P_e, P_a and P_b constant in time, the problem admits a steady solution and since $D_0 \equiv 0$, the pressure P_0 becomes an instantaneous field (i.e. $\partial_T P_0 \equiv 0$), reducing (10) to

$$\frac{\partial^2 P_0}{\partial Z^2} + BP_0 = BP_e, \tag{15}$$

with $A_1 \equiv 0$ and the constant B given in the section Methods. Considering that B is always negative, i.e. $|B| = -B$, the solution of (15) is of the form

$$P_0 = P_e + \gamma_1 e^{Z\sqrt{|B|}} + \gamma_2 e^{-Z\sqrt{|B|}}, \tag{16}$$

where γ_1 and γ_2 are constants determined by applying the boundary conditions at $Z = 0$ ($P_0|_{Z=0} = P_a$) and $Z = L$ ($P_0|_{Z=L} = P_b$)

$$\gamma_1 = \frac{(P_a - P_e)e^{-L\sqrt{|B|}} - (P_b - P_e)}{e^{-L\sqrt{|B|}} - e^{L\sqrt{|B|}}}, \quad \gamma_2 = \frac{(P_b - P_e) - (P_a - P_e)e^{L\sqrt{|B|}}}{e^{-L\sqrt{|B|}} - e^{L\sqrt{|B|}}}. \tag{17a}$$

For validation purpose, the numerical solution of (10) for $E_e = 10^5$, $P_e = 2$, $P_a = 5$, $P_b = 0$, $M_e = 1$, $\bar{H} = 0$, $L = 5$ and $R_1 = 5$ at $t = 1$ is compared with the exact solution (16), valid only for $E_e \to \infty$ and $\bar{H} = 0$. The very good agreement is depicted in Fig. 2.

A further confirmation of the derivation of our model is provided in the limit of large inner radius R_1. For $R_1 \to \infty$, the curvature effect becomes negligible and (15) tends to the equation for the incompressible flow in a plane shallow channel with a permeable wall

$$\frac{\partial^2 P_0}{\partial X^2} - 12M_e P_0 = -12M_e P_e, \tag{18}$$

where the non-dimensional plane coordinates are $\vec{X} = (X, Y)$. Equation (18) is derived in the section Methods and it implies that $\lim_{R_1 \to \infty} 1/B_0 = -12$. The correct asymptotic limit of our model is retrieved, as shown in Fig. 3.

Fixing $P_e = P_b = 0$ and $P_a = 10^{-3}$ the pressure in the annular pipe reads:

$$P_0 = P_a \frac{e^{(Z-L)\sqrt{|B|}} - e^{(L-Z)\sqrt{|B|}}}{e^{-L\sqrt{|B|}} - e^{L\sqrt{|B|}}}, \tag{19}$$

hence, the solution is nothing but an exponential relaxation from P_a to $P_e = P_b = 0$. This same trend is observed for all the cases with $\bar{H} = 0$, and they are compared in Fig. 4 for $M_e = 1$ and $E_e = 0.01$, 0.1 and 1 at $t = 50$. Since the annular channel flow is a limit for $E_e \to \infty$ (i.e. $D_0 \to 0$), upon an increase of stiffness of the brain tissue, the pressure distribution tends to (19). It is remarkable that, for the least rigid brain tissue, i.e. $E_e = 0.01$, the exponential relaxation of P_0, D_0 and U_e blends soon (i.e. approximately for $Z > 0.5$) with a linear trend which holds in most of the thin film.

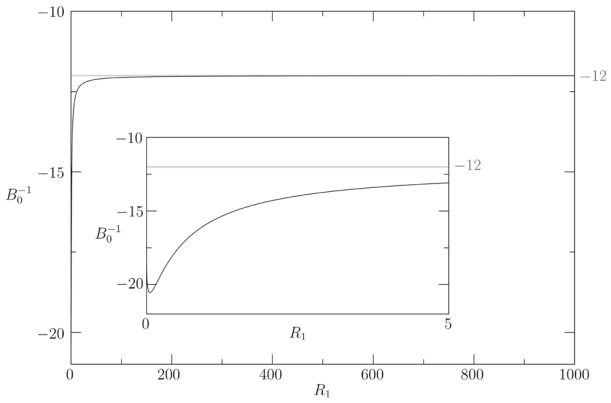

Figure 3. Asymptotic limit of $1/B_0$ to match the plane flow coefficient for $R_1 \to \infty$: $\lim_{R_1\to\infty} 1/B_0 = -12$.

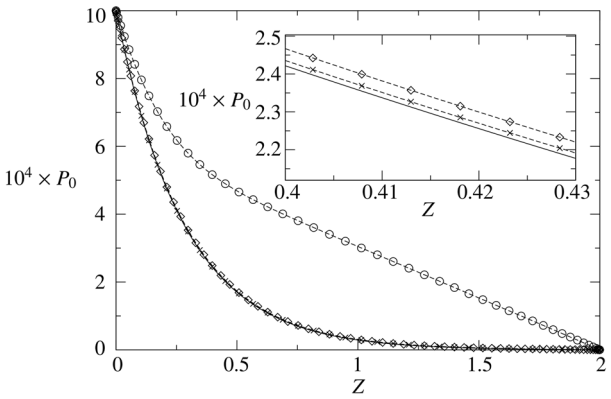

Figure 4. Pressure distribution in a rigid pipe with a permeable wall (solid line) compared to the pressure in the PVS for $\bar{H} = 0$, $E_e = 0.01$ (circles and dashed-line), 0.1 (squares and dashed-line) and 1 (crosses and dashed-line). In all the cases $M_e = 1$, $L = 2$, $R_1 = 10$ (i.e. $B_0 = -0.079557$), $P_e = P_b = 0$ and $P_a = 10^{-3}$ at $t = 50$.

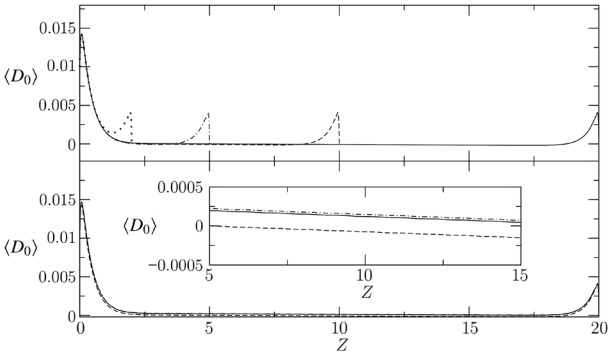

Figure 5. Top: Effect of PVS length for $\bar{H} = 0.2$, $R_1 = 10$, $M_e = 1$, $E_e = 0.1$ is investigated considering four axial lengths: $L = 2$ (dotted), $L = 5$ (dashed–dotted), $L = 10$ (dashed), $L = 20$ (solid). Bottom: Effect of curvature for $\bar{H} = 0.2$, $L = 20$, $M_e = 0.5$, $E_e = 0.1$ investigated considering three inner radii: $R_1 = 10$ (solid line), $R_1 = 100$ (dashed line) and $R_1 = 1000$ (dashed–dotted line).

Effect of gap length. The effect of the gap length L is investigated, setting $\bar{H} = 0.1$, $R_1 = 10$, $M_e = 0.5$, $E_e = 0.1$ and varying $L \in [2,\ 20]$. Four PVS lengths are considered and the corresponding average deformation $\langle D_0 \rangle$ is depicted in the top panel of Fig. 5: $L = 2$ (dotted), $L = 5$ (dashed–dotted), $L = 10$ (dashed), $L = 20$ (solid). For all the curves it is noticed that the boundary effect which dominates the average deformation distribution is limited to a couple of wavelengths from the boundaries.

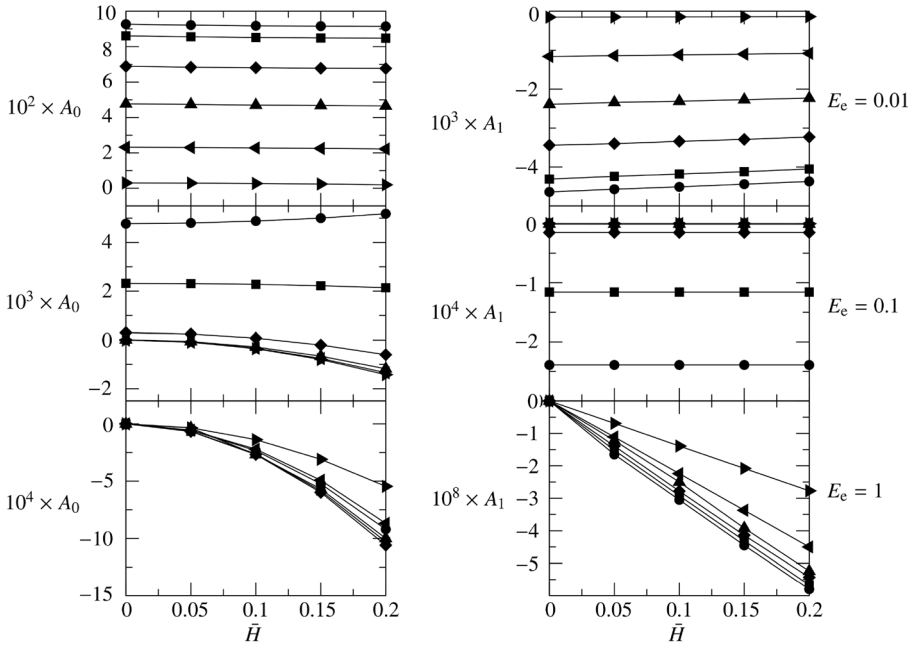

Figure 6. A_0 (left panels) and A_1 (right panels) coefficients for the average deformation $\langle D_0 \rangle$ for $R_1 = 10$, $L = 20$, $M_e \in [0.1,\ 5]$, and $E_e = 0.01$ (top), $E_e = 0.1$ (middle) and $E_e = 1$ (bottom). Six values of M_e are considered: $M_e = 0.1$ (●), 0.2 (■), 0.5 (◆), 1 (▲), 2 (◀), 5 (▶).

The peak at $Z = 0$ is well understood considering the equivalence $P_0 = E_e^{-1} D_0$, which therefore fixes a steady Dirichlet boundary condition on $D_0(Z = 0) = E_e P_a$, hence $\langle D_0 \rangle (Z = 0) = E_e P_a$. This value is much larger than the average deformation in the bulk, since the flow in the bulk is strongly influenced by the permeability of the glial boundary (see Fig. 4). The second peak near $Z = L$ is typical of non-transparent boundary conditions for wave propagation problems; the steep negative gradient of $\langle D_0 \rangle (Z \to L)$ is a direct results of the Dirichlet boundary condition $D_0(Z = L) = E_e P_b = \langle D_0 \rangle (Z = L) = 0$.

In order to get rid of these boundary effects induced by the simplified pressure boundary conditions, we focus on the bulk area where each curve can be well approximated by a straight line, characterized by the only two coefficients A_0 and A_1

$$\langle D_0 \rangle |_{Z \in [5, L-5]} \approx A_0 + A_1 Z. \tag{20}$$

where the coefficient A_0 represents the time- and space-averaged brain tissue deformation and the coefficient A_1 is the time-averaged axial rate of change of the brain tissue deformation. It is further noticed that the average through flow $\langle U_e \rangle$ (derived by $\langle D_0 \rangle$ multiplying by $M_e E_e$) admits a steady streaming since $\int_5^{L-5} \langle U_e \rangle dZ \neq 0$. The characterization of the steady streaming via A_0 and A_1 is one of the main aim of our study, as reported in the followings.

Effect of curvature. The effect of the curvature is discussed, setting $\bar{H} = 0.1$, $L = 20$, $M_e = 0.5$, $E_e = 0.1$ and varying $R_1 \in [10,\ 1000]$. The bottom panel of Fig. 5 compares the average deformation for the three radii of curvature $R_1 = 10$ (solid line), $R_1 = 100$ (dashed line) and $R_1 = 1000$ (dashed–dotted line). The curvature of the annular PVS has relatively small importance in terms of $\langle D_0 \rangle$. Increasing the curvature ($\downarrow R_1$) does not have a monotonic trend on the average deformation in the middle of the liquid film, and it tends to preserve the peak near the inflow and outflow boundaries. As also confirmed by Fig. 3, which plots the asymptotic limit of B_0^{-1}, the curvature effect becomes negligible when comparing $R_1 = 100$ and $R_1 = 1000$.

Highest curvature ($R_1 = 10$) and longest perivascular gap ($L = 20$). The following results consider $R_1 = 10$ and $L = 20$. The effect of the peristaltic wave amplitude $\bar{H} \in [0, 0.2]$ and of the brain tissue permeability $M_e \in [0.1, 5]$ is investigated for three cases: soft ($E_e = 0.01$), medium-stiff ($E_e = 0.1$) and rigid ($E_e = 1$) brain tissue.

Soft brain tissue. The results of A_0 (left-top panel) and A_1 (right-top panel) for $E_e = 0.01$ are depicted in Fig. 6. Five values of $\bar{H}$ are considered, i.e. $\bar{H} = 0$, 0.05, 0.1, 0.15, and 0.2, for each six values of M_e: $M_e = 0.1$ (●), 0.2 (■), 0.5 (◆), 1 (▲), 2 (◀), 5 (▶). The case $\bar{H} = 0$ is the only one admitting a steady state for the flow. This reflects on the time-average deformation $\langle D_0 \rangle$ (and on $\langle P_0 \rangle$ and $\langle U_e \rangle$, see (14)), which has an exponential trend matching to a linear profile (see Fig. 4). Moreover, all the cases considered, regardless of M_e, E_e and $\bar{H}$, show a decrease of $\langle D_0 \rangle$, $\langle P_0 \rangle$ and $\langle U_e \rangle$ as Z increases, i.e. A_1 is always negative. Upon an increase of $\bar{H}$, also the amplitude of the

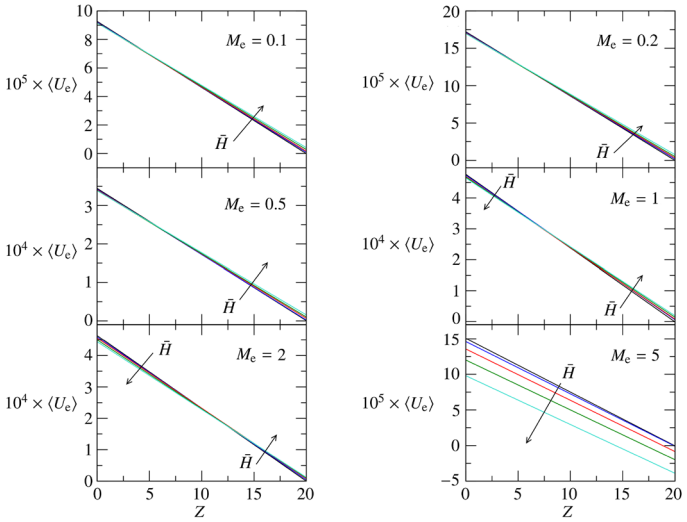

Figure 7. $\langle U_e \rangle$ for $R_1 = 10$, $L = 20$, $M_e \in [0.1,\ 5]$, and $E_e = 0.01$. Five values of $\bar{H}$ are considered: $\bar{H} = 0$ (black), 0.05 (blue), 0.1 (red), 0.15 (green), 0.2 (cyan).

average brain tissue deformation $\langle D_0 \rangle$ increases ($A_1 \uparrow$). The coefficient A_0 is monotonically decreasing with $\bar{H}$, even if almost negligibly. For soft brain tissues, A_0 and A_1 strongly depend on the permeability of the brain tissue M_e. For the parameter ranges investigated, A_1 and A_0 show a monotonic trend decreasing as M_e increases, if $E_e = 0.01$.

Employing the equivalence $U_e = E_e M_e D_0$, the coefficients A_0 and A_1 are used to plot the fitting approximation of $\langle U_e \rangle$. For soft brain tissues, Fig. 7 reports the time average of the through-flow profile across the glial boundary for $M_e \in [0.1,\ 5]$ and $\bar{H} \in [0, 0.2]$. Each panel of Fig. 7 compares the effect of the peristaltic wave amplitude (black: $\bar{H} = 0$; blue: $\bar{H} = 0.05$; red: $\bar{H} = 0.1$; green: $\bar{H} = 0.15$; cyan: $\bar{H} = 0.2$) keeping constant the permeability parameter M_e for $E_e = 0.01$. Figure 7 demonstrates that a steady through flow is due to the peristaltic wave amplitude, which increases the overall through flow, $\int_0^L \langle U_e \rangle dZ$, for $M_e \leq 1$ and decreases it for $M_e > 1$.

The understanding of a steady streaming component in the through flow is an interesting outcome of our model. In fact, considering that H is a zero-mean deformation, the increase of $\langle P_0 \rangle = E_e \langle D_0 \rangle$ with $\bar{H}$ highlights the steady pressure component induced by the traveling wave. This is possible only because the brain tissue is deformable $E_e \not\to \infty$, hence $\partial_T D_0 = E_e^{-1} \partial_T P_0 \neq 0$. The presence of a time-derivative in (10) allows a phase shift between D_0 and H. To better understand it, let us consider the case of $E_e \to \infty$ with $\bar{H} \neq 0$. Since the lubrication approximation considers only linear terms of the momentum equation, if $E_e \to \infty$, $\partial_T D_0 = E_e^{-1} \partial_T P_0 = 0$ and (10) becomes an instantaneous equation. As a consequence, for $E_e \to \infty$, the fluid flow becomes fully reversible in time and a symmetric zero-mean deformation H, as the one we consider, would produce a zero-mean streaming $\langle U_e \rangle \equiv 0$ within a traveling wave period. For $E_e \not\to \infty$, the time derivative $\partial_T P_0$ carries the memory of the previous states and makes the flow non-reversible in time, which allows for steady streaming.

Medium-stiff brain tissue. The results for $E_e = 0.1$ are depicted in Fig. 6: A_0 (left-middle panel) and A_1 (right-middle panel). The same line-style coding is used to denote different $\bar{H}$, as for the soft tissue case. The first difference with the soft-tissue case is observed in A_0, which is one to two orders of magnitude lower than for soft brain tissues. Once again, this is understood considering the steady case ($\bar{H} = 0$), which reduced to an almost-exponential relaxation profile (see squares in Fig. 4). Hence, the linear profile inherited by soft tissues from $\bar{H} = 0$ vanished for medium-stiff brain tissues reducing A_0 of two orders of magnitudes. The increased rigidity E_e further contributes to this reduction of A_0 as $D_0 = P_0 E_e^{-1}$. Differently from the soft-tissue case, for $E_e = 0.1$, A_0 shows a certain dependence on $\bar{H}$, which grows monotonically for small permeability parameters $M_e = 0.1$ and decreases monotonically when the permeability of the glial boundary is higher. On the other hand, A_1 is always negative and independent (up to the accuracy of our numerical simulation) on $\bar{H}$, and it is remarkably influenced by M_e up to becoming almost zero if the permeability parameter is high enough ($M_e \gtrsim 1$). This is well understood considering that a higher M_e implies a faster relaxation of the average pressure to a constant value, as indicated by the coefficient B of (19). Since $P_0 = U_e M_e^{-1} = D_0 E_e$, this same consideration applies to $\langle D_0 \rangle$ and $\langle U_e \rangle$.

The hallmark of the steady exponential relaxation due to the pressure gradient is hardly visible when comparing the time-dependent profiles of D_0 for $\bar{H} = 0$ and $\bar{H} = 0.4$. This is the direct consequence of the stiffness parameter, since increasing E_e reduces the deformation at $Z = 0$ for a given P_a, i.e. $D_0|_{Z=0} = E_e^{-1} P_a$. The flow is then dominated by the peristaltic wave deformation H which gives rise to an interesting phenomenon: increasing the permeability parameter M_e, for very permeable brain tissues $M_e \gtrsim 1$, the average brain tissue deformation $\langle D_0 \rangle$ becomes negative.

As a result, using (14), a negative average deformation $\langle D_0 \rangle < 0$ implies a suction from the brain to the perivascular space $\langle U_e \rangle < 0$. Hence, increasing M_e gives rise to an opposite direction of the steady streaming,

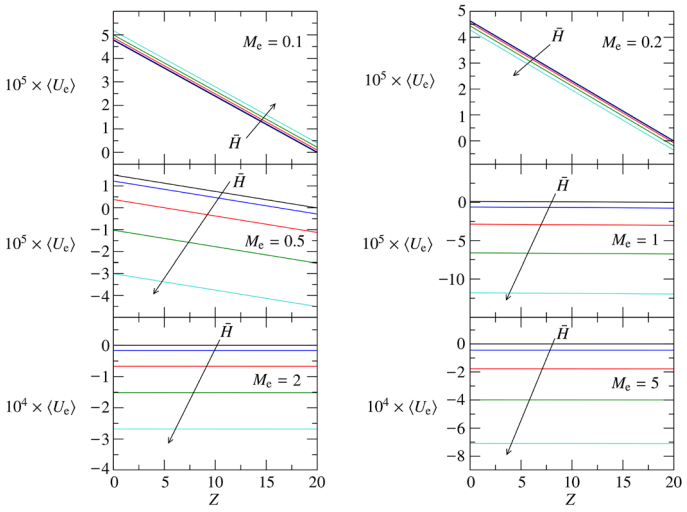

Figure 8. $\langle U_e \rangle$ for $R_1 = 10$, $L = 20$, $M_e \in [0.1,\ 5]$, and $E_e = 0.1$. Five values of $\bar{H}$ are considered: $\bar{H} = 0$ (black), 0.05 (blue), 0.1 (red), 0.15 (green), 0.2 (cyan).

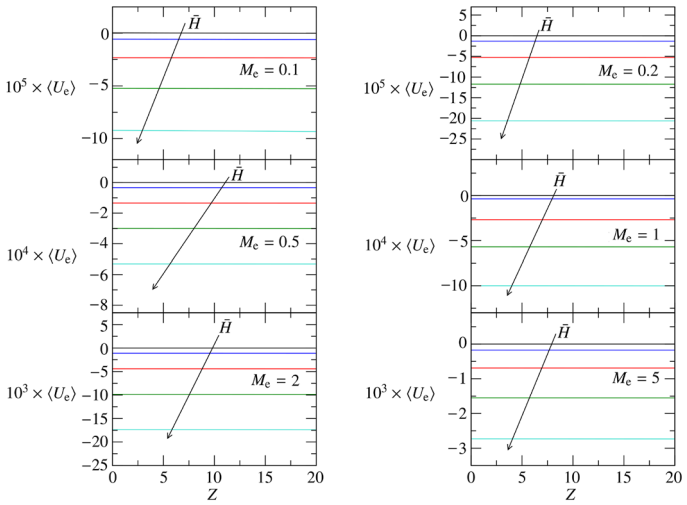

Figure 9. $\langle U_e \rangle$ for $R_1 = 10$, $L = 20$, $M_e \in [0.1,\ 5]$, and $E_e = 1$. Five values of $\bar{H}$ are considered: $\bar{H} = 0$ (black), 0.05 (blue), 0.1 (red), 0.15 (green), 0.2 (cyan).

which now flows from the brain to the PVS. Based on Fig. 6, the sign change occurs at $M_e \approx 0.5$ for $\bar{H} \geq 0.15$ and at $M_e \approx 1 \forall \bar{H}$. Figure 8 reports the time average of the through-flow profile for $E_e = 0.1$, $M_e \in [0.1,\ 5]$ and $\bar{H} \in [0, 0.2]$. The same color coding of Fig. 7 is used. For medium-stiff brain tissues, an increase of the peristaltic wave frequency increases $\langle U_e \rangle$ if $M_e = 0.1$ and decreases $\langle U_e \rangle$ if $M_e \geq 0.2$, consistently with the trend of A_0 for $E_e = 0.1$.

Rigid brain tissue. The results for $E_e = 1$ are depicted in Fig. 6: A_0 (left-bottom panel) and A_1 (right-bottom panel) using the same line-style coding of the previous cases. Very similar qualitative considerations done for the medium-stiff brain tissue about $\langle D_0 \rangle$ and $\langle U_e \rangle$ apply to the rigid brain tissue. Upon an increase of E_e, the amplitude of the average deformation $\langle D_0 \rangle$ decreases (as expected, see absolute values of A_0 and A_1). Indeed, we remark that $\langle D_0 \rangle$ must become steady and converge to zero if the rigidity of the brain tissue goes to infinite, i.e. $\lim_{E_e \to \infty} \langle D_0 \rangle = \lim_{E_e \to \infty} D_0 = 0$. It is furthermore remarkable that, for $E_e = 1$, the rigidity of the brain tissue further contributes to creating negative deformation regions resulting in $\langle D_0 \rangle$ always negative. This has corresponding implications on $\langle U_e \rangle$, which admits more and more extended suction regions, making permeable stiff brain tissues streaming fluid, in average, exclusively from the glial boundary to the perivascular space. This is clearly demonstrated by Fig. 9, where the average through flow across the glial boundary is depicted using the same template of Figs. 7 and 8.

The trend reported in Fig. 6 for A_0 has an interesting minimum at about $M_e \approx 0.5$. Indeed, the integral balance $A_0 \approx \int_0^L D_0 dZ$ becomes smaller and smaller, in absolute value, upon an increase of M_e, if $M_e \geq 0.5$. This behavior is understood considering the competition between two opposite effects: (a) increasing the permeability of the glial boundary, more fluid can go through the brain tissue $|\langle U_e \rangle| \uparrow$ (see Fig. 9), hence increasing $|\langle D_0 \rangle|$, and (b) increasing the permeability parameter M_e the brain tissue will oppose less and less resistance to be penetrated, hence $|\langle D_0 \rangle| \downarrow$. The first effect is dominant for $M_e \leq 0.5$, and the absolute value of A_0 increases with M_e; the second effect is more important for $M_e \geq 1$. As a result, the deformation of the brain tissue reduces in amplitude more and more, if the permeability parameter $M_e \geq 1$, up to asymptotically leading to an undeformed brain tissues, i.e. $\lim_{M_e \to \infty} \langle D_0 \rangle = \lim_{M_e \to \infty} D_0 = 0$. Since A_1 is always four orders of magnitude smaller than A_0, the linear component of $\langle P_0 \rangle$, $\langle D_0 \rangle$ and $\langle U_e \rangle$ can safely be neglected for rigid brain tissues.

Discussion

The cerebrospinal fluid flow across the glial boundary of the brain tissue has been investigated by means of a tribological model derived from first principles. We demonstrate that the phase shift between the arterial peristaltic wave and the glial boundary deformation is a necessary conditions to break the flow symmetry and have a steady streaming. Depending on the elasticity and permeability parameters of the glial boundary, E_e and M_e, the steady streaming either enters or exits the brain. For physiologically relevant parameters, we proved that such flow is almost insensitive to curvature effects of the annular perivascular gap for $R_1 > 10$, and of the perivascular length if $L > 5$. A very comprehensive characterization of the through flow across the glial boundary is provided within our model framework, quantifying the leading order pressure $\langle P_0 \rangle$, deformation $\langle D_0 \rangle$ and through flow $\langle U_e \rangle$ across the glial boundary, averaged in time. A reduced order model can be readily derived for such quantities from our model, implementing the fitting functions $\langle P_0 \rangle \approx E_e(A_0 + A_1 Z)$, $\langle D_0 \rangle \approx A_0 + A_1 Z$ and $\langle U_e \rangle \approx E_e M_e (A_0 + A_1 Z)$ for whatever perivascular space with $R_1 > 10$ and $L > 5$.

Among the major outcomes of our study, we estimate the average leak flow velocity for a large physiologically relevant parameter space, finding that $\langle U_e \rangle$ ranges between $-0.0027 \leq \langle U_e \rangle \leq 0.0005$. Considering that typical peristaltic wave frequencies are $\omega \approx 5$ Hz, the dimensional average through flow is between $-0.0135b$ $\mathrm{s}^{-1} \leq \langle \omega b U_e \rangle \leq 0.0025b$ s^{-1}, where $10^{-6} \leq b \leq 1.5 \times 10^{-4}$ m is the thickness of the perivascular space. Hence, our model estimates that -2.25 μm/s $\leq \langle \omega b U_e \rangle \leq 0.4$ μm/s. We remark that this result is consistent with experimental measurements and other model results, since $\langle \omega b U_e \rangle$ is typically some orders of magnitude smaller than $\max_t \omega b U_e$, which is supposed to be in the range of $1\ \mu\mathrm{m/s} \leq \max_t \omega b U_e \leq 100\ \mu\mathrm{m/s}$. In particular, considering CSF transport in the perivascular space, Faghih and Sharp[15] also mention that arterial pulsations can account for the physiological flow rates through these high flow-resistant spaces. Overall, our model elucidates the dependence of CSF transport on the factors listed in Table 1, and therefore provides a framework to better understand the effect of physiological parameters on perivascular transport. For example, the model can be used to predict how pathologies known to modify parameters like extracellular matrix stiffness (e.g. glial scarring following central nervous system injury) alter the magnitude and direction of CSF flow. Therefore, in addition to calculating specific flow rates, the model described here improves our conceptual understanding of perivascular transport in the brain.

A few concluding remarks about the model robustness and its possible extensions. Owing to the very small values of the non-dimensional film thickness, i.e. $0.000001 < \varepsilon < 0.0375$ (see Table 1), the thin-film approximation represents the most insightful and numerically robust leading-order model for Newtonian creeping flows with a permeable boundary. If we consider the complete axisymmetric creeping flow model, the pressure would depend on both coordinates, R and Z. Still, as $\varepsilon \ll 1$, the pressure would be a very weak function of R, and passing from the thin-film to the complete creeping flow model would mean a significant increment of the model complexity with negligible advantages at leading-order. On the other hand, assuming that the P does not depend on R, as the simplification (6a) does, does not lead to remarkable model inaccuracies. On top of it, owing to the small ε, solving numerically the creeping flow equations is a much more challenging task than solving the thin-film equations because the creeping flow system becomes stiffer and stiffer the smaller ε is. In a recent paper, Ladron-de-Guevara et al.[31] point out that a correct modeling of the outflow boundary condition is important when one wants to model perivascular pumping. We further stress that our model does not include any restrictive assumption on the kind of boundary conditions that can be considered. In fact, the extension of the model to pulsatile boundary conditions is straightforwardly achieved by replacing (7a) and (7b) by $Z = 0 : P_0 = P_a(t)$ and $Z = L : P_0 = P_b(t)$. We further remark that including the pulsatile nature of the boundary conditions can induce an improvement of the model accuracy, and we propose it as a very relevant objective for future studies.

Methods

Analytic details. Plugging the asymptotic expansion (5) into (3), it yields

$$\varepsilon^3 \,\mathrm{Re}\left[\frac{\partial U_0}{\partial T} + U_0\frac{\partial U_0}{\partial R} + W_0\frac{\partial U_0}{\partial Z} + \varepsilon\left(\frac{\partial U_1}{\partial T} + U_1\frac{\partial U_0}{\partial R} + U_0\frac{\partial U_1}{\partial R} + W_1\frac{\partial U_0}{\partial Z} + W_0\frac{\partial U_1}{\partial Z}\right) + \mathcal{O}(\varepsilon^2)\right] = -\frac{\partial P_0}{\partial R} - \varepsilon\frac{\partial P_1}{\partial R} + \mathcal{O}(\epsilon^2), \tag{21a}$$

$$\varepsilon\,\mathrm{Re}\left[\frac{\partial W_0}{\partial T}+U_0\frac{\partial W_0}{\partial R}+W_0\frac{\partial W_0}{\partial Z}+\varepsilon\left(\frac{\partial W_1}{\partial T}+U_1\frac{\partial W_0}{\partial R}+U_0\frac{\partial W_1}{\partial R}+W_1\frac{\partial W_0}{\partial Z}+W_0\frac{\partial W_1}{\partial Z}\right)+\mathcal{O}(\varepsilon^2)\right]$$
$$=-\frac{\partial P_0}{\partial Z}-\varepsilon\frac{\partial P_1}{\partial Z}+\frac{1}{R}\frac{\partial W_0}{\partial R}+\frac{\varepsilon}{R}\frac{\partial W_1}{\partial R}+\frac{\partial^2 W_0}{\partial R^2}+\varepsilon\frac{\partial^2 W_1}{\partial R^2}+\mathcal{O}(\varepsilon^2), \tag{21b}$$

$$\frac{1}{R}\left[\frac{\partial(RU_0)}{\partial R}+\varepsilon\frac{\partial(RU_1)}{\partial R}\right]+\frac{\partial W_0}{\partial Z}+\varepsilon\frac{\partial W_1}{\partial Z}+\mathcal{O}(\varepsilon^2)=0. \tag{21c}$$

Expanding the boundary conditions (4) leads

$$Z=0:\quad P_0+\varepsilon P_1+\mathcal{O}(\varepsilon^2)=P_a, \tag{22a}$$

$$Z=L:\quad P_0+\varepsilon P_1+\mathcal{O}(\varepsilon^2)=P_b, \tag{22b}$$

$$R=R_1+H:\quad U_0+\varepsilon U_1+\mathcal{O}(\varepsilon^2)=\partial_T H, \tag{22c}$$

$$W_0+\varepsilon W_1+\mathcal{O}(\varepsilon^2)=0, \tag{22d}$$

$$\begin{aligned}
R=R_1+1+D:\quad \vec{n}=(n_z,n_r)&=\frac{\left[-\varepsilon\partial_Z D_0+\mathcal{O}(\varepsilon^2),1\right]}{\sqrt{1+\varepsilon^2(\partial_Z D_0)^2+\mathcal{O}(\varepsilon^3)}},\\
\vec{t}=(t_z,t_r)&=\frac{\left[1,\varepsilon\partial_Z D_0+\mathcal{O}(\varepsilon^2)\right]}{\sqrt{1+\varepsilon^2(\partial_Z D_0)^2+\mathcal{O}(\varepsilon^3)}},\\
\frac{U_0+\varepsilon U_1-\varepsilon\partial_Z D_0 W_0+\mathcal{O}(\varepsilon^2)}{\sqrt{1+\varepsilon^2(\partial_Z D_0)^2+\mathcal{O}(\varepsilon^3)}}&=M_e\big(P_0+\varepsilon P_1-P_e+\mathcal{O}(\varepsilon^2)\big)\\
&\quad+\partial_T\big(P_0+\varepsilon P_1-P_e+\mathcal{O}(\varepsilon^2)\big)/E_e,\\
W_0+\varepsilon W_1+\varepsilon U_0\partial_Z D_0+\mathcal{O}(\varepsilon^2)&=0,\\
D_0+\varepsilon D_1+\mathcal{O}(\varepsilon^2)&=\big(P_0+\varepsilon P_1+\mathcal{O}(\varepsilon^2)-P_e\big)/E_e,
\end{aligned} \tag{22e}$$

If $\mathrm{Re}\ =\mathcal{O}(1)$ or smaller, the leading order continuity and Navier–Stokes equation read

$$\frac{\partial P_0}{\partial R}=0, \tag{23a}$$

$$\frac{\partial P_0}{\partial Z}=\frac{1}{R}\frac{\partial W_0}{\partial R}+\frac{\partial^2 W_0}{\partial R^2}, \tag{23b}$$

$$\frac{1}{R}\frac{\partial(RU_0)}{\partial R}+\frac{\partial W_0}{\partial Z}=0. \tag{23c}$$

The system (23) is completed by the boundary conditions at leading order

$$Z=0:\quad P_0=P_a, \tag{24a}$$

$$Z=L:\quad P_0=P_b, \tag{24b}$$

$$R=R_1+H:\quad U_0=\partial_T H,\qquad W_0=0, \tag{24c}$$

$$\begin{aligned}
R=R_1+1+D:\quad \vec{n}&=(n_z,n_r)=(0,1),\\
\vec{t}&=(t_z,t_r)=(1,0),
\end{aligned} \tag{24d}$$

$$U_0=M_e(P_0-P_e)+\frac{1}{E_e}\frac{\partial(P_0-P_e)}{\partial T}, \tag{24e}$$

$$W_0=0, \tag{24f}$$

$$D_0=\frac{P_0-P_e}{E_e}. \tag{24g}$$

Equation (23)b can be recast in the form

$$R\frac{\partial P_0}{\partial Z} = \frac{\partial}{\partial R}\left(R\frac{\partial W_0}{\partial R}\right), \tag{25}$$

keeping in mind that P_0 is just function of Z and T, and integrating in R, it yields

$$\frac{R^2}{2}\frac{\partial P_0}{\partial Z} + C_1 = R\frac{\partial W_0}{\partial R}, \tag{26}$$

where C_1 is just function of Z and T. Dividing by R and integrating once again in radial direction, it yields

$$\frac{R^2}{4}\frac{\partial P_0}{\partial Z} + C_1\ln(R) + C_2 = W_0, \tag{27}$$

which corresponds to (8), where C_2 is just function of Z and T. The leading-order boundary conditions in W_0 are $W_0|_{R=R_1+H} = 0$ and $W_0|_{R=R_1+1+D_0} = 0$. Substituting them in (27) yields

$$W_0|_{R=R_1+H} = \frac{(R_1+H)^2}{4}\frac{\partial P_0}{\partial Z} + C_1\ln(R_1+H) + C_2 = 0, \tag{28a}$$

$$W_0|_{R=R_1+1+D_0} = \frac{(R_1+1+D_0)^2}{4}\frac{\partial P_0}{\partial Z} + C_1\ln(R_1+1+D_0) + C_2 = 0. \tag{28b}$$

Subtracting the two equations, we eliminate C_2, and determine C_1

$$C_1 = \alpha\frac{\partial P_0}{\partial Z}, \qquad \alpha = \frac{(R_1+H)^2 - (R_1+1+D_0)^2}{4[\ln(R_1+1+D_0) - \ln(R_1+H)]}. \tag{29}$$

By substitution of C_1 in (28a), C_2 is determined

$$C_2 = \beta\frac{\partial P_0}{\partial Z}, \qquad \beta = -\frac{(R_1+H)^2}{4} - \alpha\ln(R_1+H), \tag{30}$$

where α and β are functions of Z and T.

Equation (23)c can be recast in the form

$$\frac{\partial(RU_0)}{\partial R} = -R\frac{\partial W_0}{\partial Z}. \tag{31}$$

Substituting (27) into (31), it reads

$$\frac{\partial(RU_0)}{\partial R} = -\frac{R^3}{4}\frac{\partial^2 P_0}{\partial Z^2} - R\ln(R)\frac{\partial C_1}{\partial Z} - R\frac{\partial C_2}{\partial Z}, \tag{32}$$

and integrating yields

$$RU_0 = C_3 - \frac{R^4}{16}\frac{\partial^2 P_0}{\partial Z^2} - \frac{R^2[2\ln(R)-1]}{4}\frac{\partial C_1}{\partial Z} - \frac{R^2}{2}\frac{\partial C_2}{\partial Z}, \tag{33}$$

where C_3 is a function of Z and T. Dividing by R, (9) is retrieved

$$U_0 = \frac{C_3}{R} - \frac{R^3}{16}\frac{\partial^2 P_0}{\partial Z^2} - \frac{R[2\ln(R)-1]}{4}\frac{\partial C_1}{\partial Z} - \frac{R}{2}\frac{\partial C_2}{\partial Z}. \tag{34}$$

Applying the leading-order boundary conditions on U_0, yields

$$U_0|_{R=R_1+H} = \frac{C_3}{R_1+H} - \frac{(R_1+H)^3}{16}\frac{\partial^2 P_0}{\partial Z^2} - \frac{(R_1+H)[2\ln(R_1+H)-1]}{4}\frac{\partial C_1}{\partial Z} - \frac{(R_1+H)}{2}\frac{\partial C_2}{\partial Z} = \frac{\partial H}{\partial T}, \tag{35a}$$

$$\begin{aligned} U_0|_{R=R_1+1+D_0} &= \frac{C_3}{R_1+1+D_0} - \frac{(R_1+1+D_0)^3}{16}\frac{\partial^2 P_0}{\partial Z^2} - \frac{(R_1+1+D_0)[2\ln(R_1+1+D_0)-1]}{4}\frac{\partial C_1}{\partial Z} - \frac{(R_1+1+D_0)}{2}\frac{\partial C_2}{\partial Z} \\ &= M_e(P_0 - P_e) + \frac{\partial D_0}{\partial T} = M_e(P_0 - P_e) + \frac{1}{E_e}\frac{\partial(P_0 - P_e)}{\partial T}. \end{aligned} \tag{35b}$$

Eliminating C_3 by combining (35a) and (35b) leads to

$$\begin{aligned} &(R_1+H)\left\{\frac{\partial H}{\partial T} + \frac{(R_1+H)^3}{16}\frac{\partial^2 P_0}{\partial Z^2} + \frac{(R_1+H)[2\ln(R_1+H)-1]}{4}\frac{\partial C_1}{\partial Z} + \frac{(R_1+H)}{2}\frac{\partial C_2}{\partial Z}\right\} = (R_1+1+D_0)\{M_e(P_0-P_e) \\ &+\frac{1}{E_e}\frac{\partial(P_0-P_e)}{\partial T} + \frac{(R_1+1+D_0)^3}{16}\frac{\partial^2 P_0}{\partial Z^2} + \frac{(R_1+1+D_0)}{2}\frac{\partial C_2}{\partial Z} + \frac{(R_1+1+D_0)[2\ln(R_1+1+D_0)-1]}{4}\frac{\partial C_1}{\partial Z}\Big\}, \end{aligned} \tag{36}$$

which is equivalent to (10). The coefficient C_3 is then computed by substituting the solution P_0 and its derivatives in (35a). The coefficients in (10) are

$$A_0 = \frac{E_e\alpha}{4}\left\{(R_1+1+D_0)[2\ln(R_1+1+D_0)-1]-\frac{(R_1+H)^2}{R_1+1+D_0}[2\ln(R_1+H)-1]\right\} + \frac{E_e\beta}{2}\left[(R_1+1+D_0)-\frac{(R_1+H)^2}{(R_1+1+D_0)}\right]+\frac{E_e}{16}\left[(R_1+1+D_0)^3-\frac{(R_1+H)^4}{R_1+1+D_0}\right], \tag{37a}$$

$$A_1 = \frac{E_e}{4}\frac{\partial\alpha}{\partial Z}\left\{(R_1+1+D_0)[2\ln(R_1+1+D_0)-1]-\frac{(R_1+H)^2}{R_1+1+D_0}[2\ln(R_1+H)-1]\right\} + \frac{E_e}{2}\frac{\partial\beta}{\partial Z}\left[(R_1+1+D_0)-\frac{(R_1+H)^2}{(R_1+1+D_0)}\right], \tag{37b}$$

$$A_2 = E_eM_e, \tag{37c}$$

$$\alpha = \frac{(R_1+H)^2-(R_1+1+D_0)^2}{4[\ln(R_1+1+D_0)-\ln(R_1+H)]}, \tag{37d}$$

$$\beta = -\frac{(R_1+H)^2}{4}-\alpha\ln(R_1+H), \tag{37e}$$

$$C_1 = \alpha\frac{\partial P_0}{\partial Z}, \tag{37f}$$

$$C_2 = \beta\frac{\partial P_0}{\partial Z}, \tag{37g}$$

$$C_3 = (R_1+H)\left\{\frac{\partial H}{\partial T}+\left[\frac{(R_1+H)^3}{16}\right]\frac{\partial^2P_0}{\partial Z^2}+\frac{R_1+H}{4}[2\ln(R_1+H)-1]\frac{\partial C_1}{\partial Z}+\left(\frac{R_1+H}{2}\right)\frac{\partial C_2}{\partial Z}\right\}. \tag{37h}$$

The coefficient B of (15) is defined by

$$B_0 = \frac{A_0|_{H=0,\,D_0=0}}{E_e} = \frac{\alpha|_{H=0,\,D_0=0}}{4}\left\{(R_1+1)[2\ln(R_1+1)-1]-\frac{R_1^2}{R_1+1}[2\ln(R_1)-1]\right\} + \frac{\beta|_{H=0,\,D_0=0}}{2}\left[(R_1+1)-\frac{R_1^2}{R_1+1}\right]+\frac{1}{16}\left[(R_1+1)^3-\frac{R_1^4}{R_1+1}\right], \tag{38a}$$

$$B_2 = \frac{A_2|_{H=0,\,D_0=0}}{E_e} = M_e, \tag{38b}$$

$$\alpha|_{H=0,\,D_0=0} = \frac{R_1^2-(R_1+1)^2}{4[\ln(R_1+1)-\ln(R_1)]}, \tag{38c}$$

$$\beta|_{H=0,\,D_0=0} = -\frac{R_1^2}{4}-\alpha\ln(R_1), \tag{38d}$$

$$B = \frac{B_2}{B_0}. \tag{38e}$$

Shallow channel with a permeable wall. If $E_e\to\infty$, $\bar{H}=0$ and $R_1\to\infty$, the flow in a shallow channel with a permeable wall represents an asymptotic limit of our thin film problem. Denoting the channel height with b and the channel length with L, if $L\gg b$, and using the scaling (2), the non-dimensional channel flow problem at leading order reads

$$\frac{\partial P_0}{\partial Y} = 0, \tag{39a}$$

$$\frac{\partial P_0}{\partial X} = \frac{\partial^2 U_0}{\partial Y^2}, \tag{39b}$$

$$\frac{\partial U_0}{\partial X} + \frac{\partial V_0}{\partial Y} = 0. \tag{39c}$$

where $\vec{X} = (X, Y)$ denotes the non-dimensional plane coordinates, P_0 and $\vec{U}_0 = (U_0, V_0)$ are the pressure and the velocity field at leading order. The system of Eqs. (39) is completed by the boundary conditions

$$V_0|_{Y=0} = 0, \tag{40a}$$

$$V_0|_{Y=1} = M_e(P_0 - P_e), \tag{40b}$$

$$U_0|_{Y=0} = 0, \tag{40c}$$

$$U_0|_{Y=1} = 0, \tag{40d}$$

$$P_0|_{X=0} = P_a, \tag{40e}$$

$$P_0|_{X=L} = P_b. \tag{40f}$$

Considering that P_0 is only function of X, and integrating the X-momentum twice in Y, it yields

$$U_0 = \frac{\partial P_0}{\partial X}\frac{Y^2}{2} + \tilde{C}_1 Y + \tilde{C}_2. \tag{41}$$

Applying the boundary conditions in Y direction, we find $\tilde{C}_1 = -1/2\ \partial_X P_0$ and $\tilde{C}_2 = 0$. Plugging $\partial_X U_0$ in the continuity equation and integrating once in Y-direction, it yields

$$V_0 = -\frac{1}{2}\frac{\partial^2 P_0}{\partial X^2}\left(\frac{Y^3}{3} - \frac{Y^2}{2}\right) + \tilde{C}_3. \tag{42}$$

Applying the boundary conditions in Y direction, we find $\tilde{C}_3 = 0$ and the following relation for P_0 holds

$$\frac{\partial^2 P_0}{\partial X^2} - 12M_e P_0 = -12M_e P_e. \tag{43}$$

Convergence test. The Navier–Stokes and continuity equation of an incompressible flow in a perivascular thin film have been reduced to the solution of an equation in the form

$$\frac{\partial f}{\partial t} + \alpha\frac{\partial f}{\partial s^2} + \beta\frac{\partial f}{\partial s} + \gamma f = \sigma, \tag{44}$$

where $\alpha = \alpha(s,t)$, $\beta = \beta(s,t)$, $\gamma = \gamma(s,t)$ and $\sigma = \sigma(s,t)$ are known functions, $s \in [0, \Lambda]$ is the space variable (Z in our thin-film flow) and $t \in [0, t_{fin}]$ denotes the time variable.

We discretize (44) in space making use of a spectral collocation method which employs Gauss–Lobatto nodes based on Chebyshev polynomials. Denoting $[D_N] \in \mathbb{R}^{N\times N}$ and $[D_N^2] \in \mathbb{R}^{N\times N}$ the first- and second-order discrete derivation matrices in space constructed using N Chebyshev–Gauss–Lobatto nodes, (44) discretized in s reads

$$\frac{\partial \vec{f}_N}{\partial t} + \vec{\alpha}_N\left([D_N^2]\vec{f}_N\right) + \vec{\beta}_N\left([D_N]\vec{f}_N\right) + \vec{\gamma}_N\vec{f}_N = \vec{\sigma}_N, \tag{45}$$

where $\vec{f}_N, \vec{\alpha}_N, \vec{\beta}_N, \vec{\gamma}_N$ and $\vec{\sigma}_N$ are $N \times 1$ arrays which gather the values of f, α, β, γ and σ at the location of the N nodes at each instant of time t. The time discretization is carried out using the implicit Euler scheme. Denoting with t_n the current time and with t_{n+1} the next instant such that $\Delta t = t_{n+1} - t_n$, the time-discrete version of (45) reads

$$\left\{[I_N]/\Delta t + \mathrm{diag}\left(\vec{\alpha}_N^{n+1}\right)[D_N^2] + \mathrm{diag}\left(\vec{\beta}_N^{n+1}\right)[D_N] + \mathrm{diag}\left(\vec{\gamma}_N^{n+1}\right)\right\}\vec{f}_N^{n+1} = \vec{\sigma}_N^{n+1} + \vec{f}_N^{n}/\Delta t, \tag{46}$$

where the superscripts n and $n+1$ denote the times t_n and t_{n+1}, respectively, $[I_N]$ is the $N \times N$ identity matrix and $\mathrm{diag}(*)$ is the diagonal matrix resulting from distributing the $N \times 1$ array $*$ along the diagonal of an $N \times N$ matrix.

To test the numerical implementation of our code, we assume

$$\alpha = -\sin[2\pi(s-t)] - 1.05, \tag{47a}$$

$$\beta = \sin[\pi(s-2t)/6], \tag{47b}$$

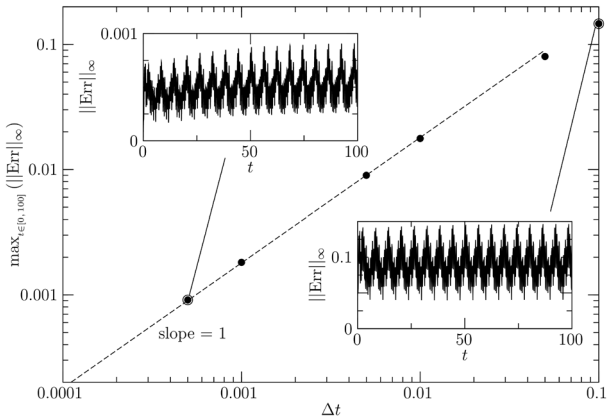

Figure 10. Maximum in time of the infinite norm of the error function ($||\mathrm{Err}||_\infty$, bullets), slope-1 line assumed as reference for the solver accuracy (dashed line). The two insets depict the infinite norm of the numerical error $||\mathrm{Err}||_\infty$ as function of t for $\Delta t = 0.1$ and 0.0005.

$$\gamma = \cos(2s), \tag{47c}$$

$$\sigma = \pi \cos[\pi(s+t)] - \alpha\pi^2 \sin[\pi(s+t)] + \beta\pi \cos[\pi(s+t)] + \gamma \sin[\pi(s+t)], \tag{47d}$$

such that the exact solution of (44) is

$$f(s,t) = \sin[\pi(s+t)]. \tag{48}$$

Dirichlet boundary conditions are derived from (48) and set at $s = 0$ and $s = \Lambda = 4$ in (46), together with the initial condition $\vec{f}_N^0 = f(\vec{s}_N, t = 0) = \sin(\pi\vec{s}_N)$. We stress that the arbitrary choices made in (47) are representative of the problem of interest in our study.

The numerical solution $\vec{f}_N$ is then compared to the exact solution at each time step by means of the infinite norm of the error function $\mathrm{Err}(t^n) = f(\vec{s}_N, t = t^n) - \vec{f}_N^n$ computed at each time point. The simulations are carried out for $t = t_{fin} = 100$ setting $N = 100$ and varying Δt. Figure 10 depicts the convergence curve of the error function, which demonstrate the correctness of our numerical code. The bullets denote the maximum in time of $||\mathrm{Err}||_\infty$, depicting it in a log-log plot against the Δt to demonstrate that the solver is first-order accurate in time (see dashed line with slope 1), as expected. The infinite norm of the numerical error $||\mathrm{Err}||_\infty$ is plotted as function of time for the largest and the smallest time step (i.e. $\Delta t = 0.1$ and 0.0005, respectively) in the two insets of fig. 10.

Code availability

The code used in this paper is an in-house developed software that will be made available upon request to the corresponding author.

Received: 10 September 2020; Accepted: 12 November 2020
Published online: 03 December 2020

References

1. Iliff, J. J., Wang, M., Liao, Y., Plogg, B. A., Peng, W., Gundersen, G. A., Benveniste, H., Vates, G. E., Deane, R., Goldman, S. A. & Nagelhus, E. A. A paravascular pathway facilitates CSF flow through the brain parenchyma and the clearance of interstitial solutes, including amyloid β. *Sci. Trans. Med.* **4**, 147–111 (2012).
2. Iliff, J. J. *et al.* Cerebral arterial pulsation drives paravascular CSF-interstitial fluid exchange in the murine brain. *J. Neurosci.* **33**, 18190–18199 (2013).
3. Hadaczek, P. *et al.* The, "perivascular pump" driven by arterial pulsation is a powerful mechanism for the distribution of therapeutic molecules within the brain. *Mol. Ther.* **14**, 69–78 (2006).
4. Mestre, H. *et al.* Flow of cerebrospinal fluid is driven by arterial pulsations and is reduced in hypertension. *Nat. Commun.* **9**, 4878 (2018).
5. Saleem, A., Qaiser, A., Nadeem, S., Ghalambaz, M. & Issakhov, A. Physiological flow of non-Newtonian fluid with variable density inside a ciliated symmetric channel having compliant wall. *Arab. J. Sci. Eng.* **1–12**, (2020).
6. Saleem, A. *et al.* Physical aspects of peristaltic flow of hybrid nano fluid inside a curved tube having ciliated wall. *Res. Phys.* **19**, 103431 (2020).
7. Saleem, A. *et al.* Mathematical computations for peristaltic flow of heated non-Newtonian fluid inside a sinusoidal elliptic duct. *Phys. Scr.* **95**, 105009 (2020).
8. Wang, P. & Olbricht, W. L. Fluid mechanics in the perivascular space. *J. Theor. Biol.* **274**, 52–57 (2011).
9. Schley, D., Carare-Nnadi, R., Please, C. P., Perry, V. H. & Weller, R. O. Mechanisms to explain the reverse perivascular transport of solutes out of the brain. *J. Theor. Biol.* **238**, 962–974 (2006).
10. Kyrtsos, C. R. & Baras, J. S. Modeling the role of the glymphatic pathway and cerebral blood vessel properties in Alzheimer's disease pathogenesis. *PLoS ONE* **10**, e0139574 (2015).

11. Ratner, V. *et al.* Cerebrospinal fluid and interstitial fluid motion via the glymphatic pathway modelled by optimal mass transport. *NeuroImage* **152**, 530–537 (2017).
12. Asgari, M., de Zélicourt, D. & Kurtcuoglu, V. Glymphatic solute transport does not require bulk flow. *Sci. Rep.* **6**, 38635 (2016).
13. Aldea, R., Weller, R. O., Wilcock, D. M., Carare, R. O. & Richardson, G. Cerebrovascular smooth muscle cells as the drivers of intramural periarterial drainage of the brain. *Front. Aging Neurosci.* **11**, 1–17 (2019).
14. Jin, B.-J., Smith, A. J. & Verkman, A. S. Spatial model of convective solute transport in brain extracellular space does not support a "glymphatic" mechanism. *J. Gen. Physiol.* **148**, 489–501 (2016).
15. Faghih, M. M. & Keith Sharp, M. Is bulk flow plausible in perivascular, paravascular and paravenous channels?. *Fluids Barriers CNS* **15**, 17 (2018).
16. Rey, J. & Sarntinoranont, M. Pulsatile flow drivers in brain parenchyma and perivascular spaces: a resistance network model study. *Fluids Barriers CNS* **15**, 20 (2018).
17. Albargothy, N. J. *et al.* Convective influx/glymphatic system: tracers injected into the CSF enter and leave the brain along separate periarterial basement membrane pathways. *Acta Neuropathol.* **136**, 139–152 (2018).
18. Xie, X. *et al.* Noninvasive intracranial pressure estimation by orbital subarachnoid space measurement: the Beijing Intracranial and Intraocular Pressure (iCOP) study. *Crit. Care* **17**, R162 (2013).
19. Sakka, L., Coll, G. & Chazal, J. Anatomy and physiology of cerebrospinal fluid. *Eur. Ann. Otorhinolary.* **128**, 309–316 (2011).
20. Lightfoot, E. N. *Transport Phenomena and Living Systems* (Wiley, New York, 1974).
21. Ichimura, T., Fraser, P. A. & Cserr, H. F. Distribution of extracellular tracers in perivascular spaces of the rat brain. *Brain Res.* **545**, 103–113 (1991).
22. Bilston, L. E., Fletcher, D. F., Brodbelt, A. R. & Stoodley, M. A. Arterial pulsation-driven cerebrospinal fluid flow in the perivascular space: a computational model. *Comput. Method. Biomech. Biomed. Eng.* **6**, 235–241 (2003).
23. Gladdish, S. *et al.* Repeatability of non-invasive measurement of intracerebral pulse wave velocity using transcranial Doppler. *Clin. Sci.* **108**, 433–439 (2005).
24. Eng, J., Hoeks, A. P. G., Brands, P. J., Willigers, J. M. & Reneman, R. S. Non-invasive measurement of mechanical properties of arteries in health and disease. *Proc. Inst. Mech. Eng. H* **213**, 195–202 (1999).
25. Bloomfield, I. G., Johnston, I. H. & Bilston, L. E. Effects of proteins, blood cells and glucose on the viscosity of cerebrospinal fluid. *Pediatr. Neurosurg.* **28**, 246–251 (1998).
26. Thorin-Trescases, N. *et al.* Diameter dependence of myogenic tone of human pial arteries: possible relation to distensibility. *Stroke* **28**, 2486–2492 (1997).
27. Baumbach, G. L., Heistad, D. D. & Siems, J. E. Effect of sympathetic nerves on composition and distensibility of cerebral arterioles in rats. *J. Physiol.* **416**, 123–140 (1989).
28. Atabek, H. B. Wave propagation through a viscous fluid contained in a tethered, initially stressed, orthotropic elastic tube. *Biophys. J.* **8**, 626–649 (1968).
29. Helton, E. S., Palladino, S. & Ubogu, E. E. A novel method for measuring hydraulic conductivity at the human blood-nerve barrier in vitro. *Microvasc. Res.* **109**, 1–6 (2017).
30. Li, G., Yuan, W. & Fu, B. M. A model for the blood-brain barrier permeability to water and small solutes. *J. Biomech.* **43**, 2133–2140 (2010).
31. Ladron-de-Guevara, A., Shang, J. K., Nedergaard, M. & Kelley, D. H. Perivascular pumping in the mouse brain: realistic boundary conditions reconcile theory, simulation, and experiment, *bioRxiv* (2020).

Acknowledgements

This work was initiated during JBG's visit to Auckland supported by the University of Auckland Vice Chancellor's Distinguished Visitor Award.

Author contributions

F.R. derived the current lubrication model based on a previous version proposed by V.S. and J.B.G. All the authors contributed to the design of the research, starting from a preliminary study of V.S. and J.B.G. F.R. programmed the numerical solver, carried out all simulations, and analyzed the data. All the authors edited the article.

Competing interests

The authors declare no competing interests.

Additional information

Correspondence and requests for materials should be addressed to F.R.

Reprints and permissions information is available at www.nature.com/reprints.

Publisher's note Springer Nature remains neutral with regard to jurisdictional claims in published maps and institutional affiliations.